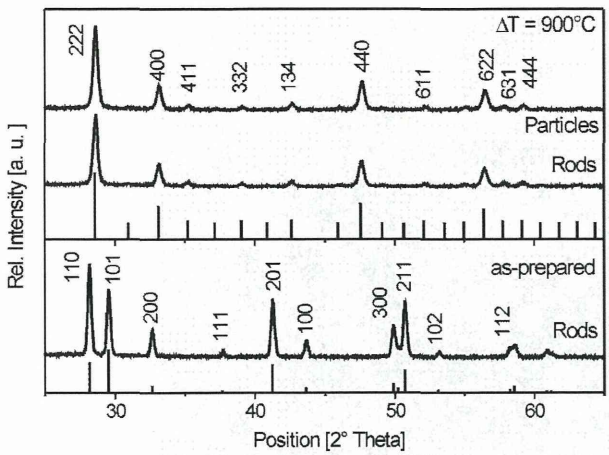

Fig. 1 X-ray diffraction patterns recorded on as-prepared and annealed (T = 900 °C, t = 30 min) nanorods by HT and particles by CTAB-assisted HP. Reference files: $Gd(OH)_3$ [83-2037], Gd_2O_3 [12-0797]

X-ray diffraction patterns recorded on samples obtained by HT and CTAB-assisted HP are shown in Fig. 1. Patterns recorded on powders obtained by surfactant-free or CTAB- and PEG-6.000-assisted HP are similar to the pattern for CTAB-assisted HP. As-prepared powders by HT consist of crystalline gadolinium hydroxide ($Gd(OH)_3$). The powders can be transformed into crystalline gadolinium oxide (Gd_2O_3) by post-thermal treatment. High annealing temperatures of 900 °C were chosen in order to remove residual water, hydroxyl or carboxylic groups that may quench photoluminescence of the Gd_2O_3:Er^{3+},Yb^{3+} nanostructures. As-prepared powders obtained by HP are amorphous, but are also transformed into crystalline Gd_2O_3 by post-thermal treatment.

The microstructure of the Gd_2O_3:Er^{3+},Yb^{3+} nanostructures was investigated by SEM. As shown in Fig. 2, HP results in spherical shape. Spheres with a diameter of an average value of 210 nm are obtained by surfactant free HP (Fig. 2a). Matijevic and Hsu [41] originally described the formation of Gd_2O_3 particles by HP. However, morphology control is difficult and larger spheres up to 300 nm in diameter or agglomerates have been observed and are described in literature [42]. Morphology and size can be controlled by the addition of surfactants. Particles with a diameter of an average value of 160 nm are obtained by addition of CTAB during HP (Fig. 2b). An average particle size of 85 nm is obtained by addition of a mixture of CTAB and PEG-6.000 (Fig. 2c). Morphology control by cationic surfactant, such as CTAB, is well known and has been described for various lanthanide containing nanostructures [43–45]. Nanostructures obtained by hydrothermal method exhibit rod like structure with lengths of an average value of 260 nm and diameters of an average value of 55 nm resulting in an average aspect ratio of 5 (Fig. 2d). As seen by XRD analysis, HT results in the formation of crystalline gadolinium hydroxide. $Gd(OH)_3$ crystallizes in the hexagonal lattice. Hence, anisotropic growth is favored and no templates are required to obtain elongated structures such as nanorods [46–49].

3.1.2 Upconversion and NIR emission

Figure 3 shows the upconversion and NIR emission spectra for particles obtained by CTAB-assisted HP (diameter: 160 nm) under excitation with 980-nm wavelength. Gd_2O_3:Er^{3+},Yb^{3+} nanostructures emit green (550 nm) and red (670 nm) luminescence (upconversion emission) as well as NIR light in the range of 1.5 μm [38]. Particles of 85 and 210 nm as well as rods show similar spectra with emission peaks at the same wavelength range.

3.2 Surface modification

Surface modification was effected under aqueous conditions with PEG-*b*-PAAc concentrations of either 0.6 mg/mL (Gd_2O_3:Er^{3+},Yb^{3+}:PEG-*b*-PAAc = 1:1) or 1.2 mg/mL (Gd_2O_3:Er^{3+},Yb^{3+}:PEG-*b*-PAAc = 1:2). Prior to the addition of 0.6 mg/mL PEG-*b*-PAAc, PEG-6.000 was added to the aqueous nanostructure dispersion in order to increase its viscosity and hereby hinder the formation of large agglomerates. Due to the positive surface charge of Gd_2O_3, confirmed by ζ-potential measurements, the polyacrylic acid group (PAAc) of the co-block polymer can be electrostatically adsorbed on the nanostructure surface. The PEG-*b*-PAAc modification of the Gd_2O_3:Er^{3+},Yb^{3+} nanostructures was confirmed by FT-IR spectra as shown in Fig. 4.

Spectra of annealed, bare nanostructures show peaks for metal-oxygen bonds in the range of 500 cm^{-1}, which confirms the formation of gadolinium oxide phase by post-thermal treatment. The presence of C=O and C–O–C bands can be assigned to impurities, such as residual carbonates resulting from an incomplete decomposition of the original precipitated $Gd(OH)CO_3 \cdot H_2O$ particles to Gd_2O_3, H_2O and CO_2 [41]. Those carbonates are extremely difficult to remove and could also be found in analogous yttria nanoparticles annealed at 900 °C [50]. Further, CO_2 from the atmosphere can absorb on the particle surface due to the basic character of Gd_2O_3 [22]. After surface modification peaks appear at 2900, 1500 and 1100 cm^{-1}. Those are referred to C–H bonds, C=O bonds in PAAc and C–O–C bond in PEG. Higher PEG-*b*-PAAc concentration results in higher intensity of those peaks. However, we suggest that lower concentration is sufficient for a successful surface modification. The broad band in the range 3,500 cm^{-1} is

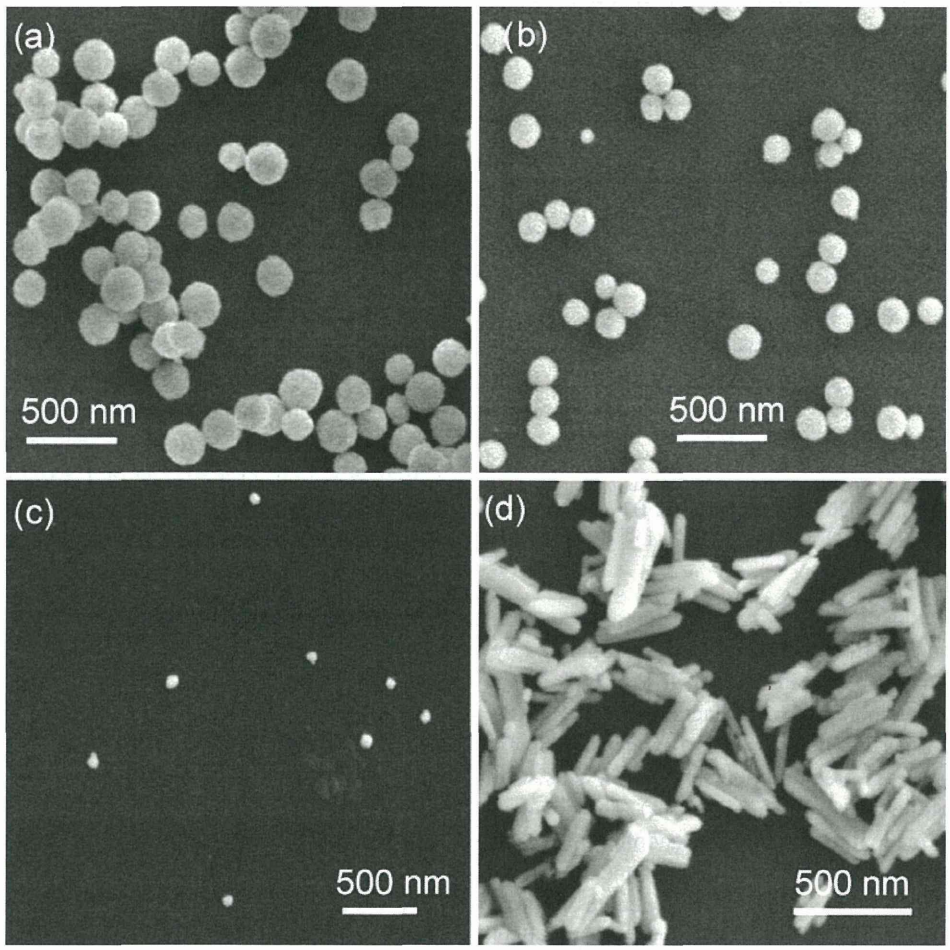

Fig. 2 Scanning electron micrographs of $Gd_2O_3:Er^{3+}Yb^{3+}$ nanostructures obtained by **a** surfactant-free ($\langle d_{SEM} \rangle = 209 \pm 28$ nm), **b** CTAB-assisted ($\langle d_{SEM} \rangle = 158 \pm 23$ nm) and **c** CTAB- and PEG-6.000-assisted HP ($\langle d_{SEM} \rangle = 86 \pm 12$ nm) as well as **d** HT ($\langle d_{SEM} \rangle = 53 \pm 18$ nm, $\langle l_{SEM} \rangle = 262 \pm 91$ nm, $\langle l/d_{SEM} \rangle = 5 \pm 1.6$)

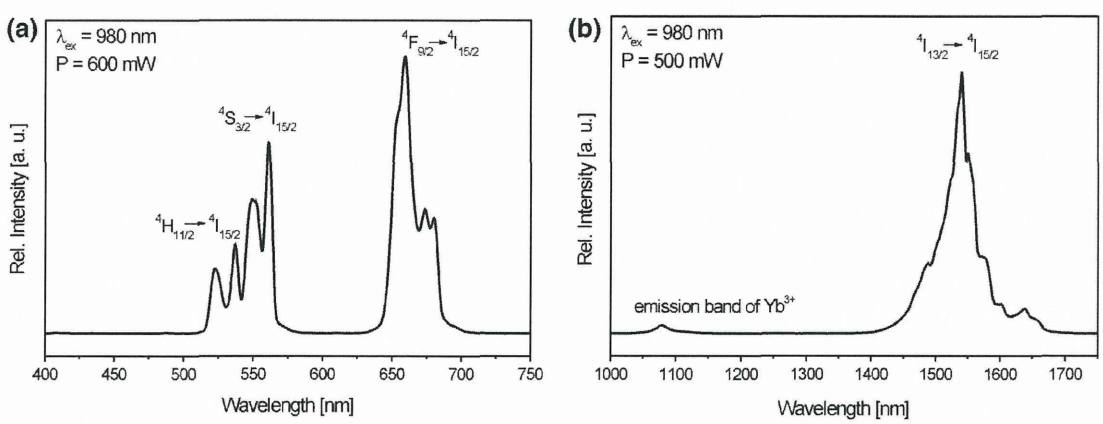

Fig. 3 **a** Upconversion and **b** NIR emission spectra recorded on $Gd_2O_3:Er^{3+},Yb^{3+}$ particles obtained by CTAB-assisted HP (*P* laser power at the source point)

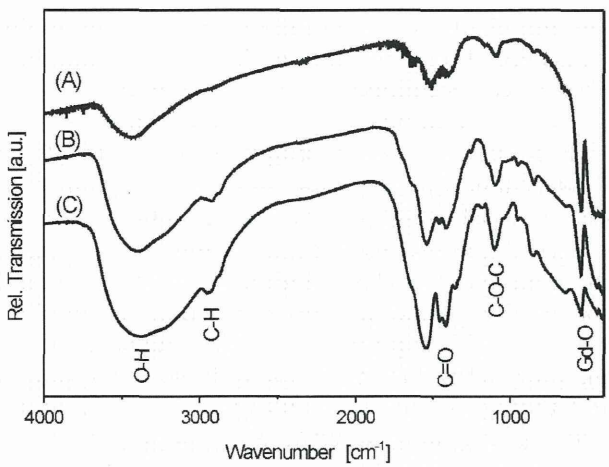

Fig. 4 FT-IR spectra of bare (*A*) and PEG-*b*-PAAc modified (*B*: c(PEG-*b*-PAAc) = 0.6 mg/mL, PEG-6.000 assisted; *C*: c(PEG-*b*-PAAc) = 1.2 mg/mL) Gd_2O_3:Er^{3+},Yb^{3+} nanostructures obtained by CTAB-assisted HP (analogous spectra were recorded on all other samples)

assigned to O–H groups originating from surface modification in aqueous medium.

3.2.1 *Dynamic light scattering*

The size distributions of PEG-*b*-PAAc modified nanostructures dispersed in water are displayed in Fig. 5 suggesting that the modified nanoparticles are well dispersed in aqueous solutions. The hydrodynamic mean diameters are 260, 190 and 90 nm for particles obtained by HP, by CTAB-assisted HP and CTAB- and PEG-6.000-assisted HP. Those values are in good agreement with particle sizes observed in SEM (210, 160 and 85 nm). In case of nanorods (SEM: 260 × 55 nm) the measured hydrodynamic mean diameter is 500 nm indicating a tendency to form agglomerations. It must also be mentioned that DLS is a standard technique for the investigation of spherical structures, while in case of rod-like structures the assumption that all particles are spherical is not valid and their analysis is much more complex. Due to Brownian motion particles move randomly, whereas elongated structures move rapidly in the elongated direction, but slowly in the other direction. During the DLS measurement an average over those rapid and slow movements of the rods over time is recorded and an equivalent sphere is calculated [51, 52]. Therefore, the hydrodynamic size can differ significantly from the true size of the structures as observed in SEM.

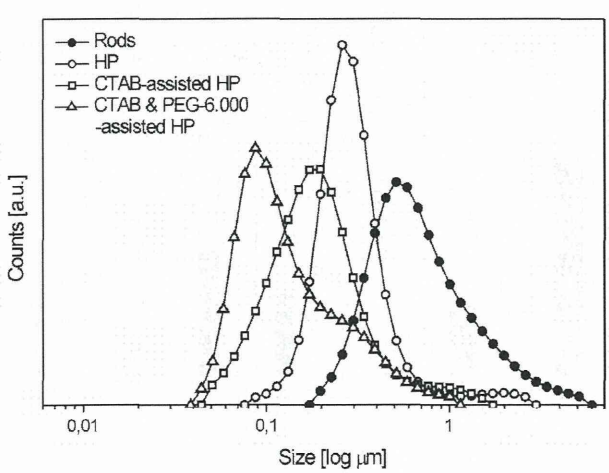

Fig. 5 Hydrodynamic diameter distribution of the PEG-*b*-PAAc modified Gd_2O_3:Er^{3+},Yb^{3+} nanostructures obtained by surfactant-free (*open circle*), CTAB-assisted (*open square*), CTAB- and PEG-6.000-assisted HP (*open triangle*) and HT (*filled circle*)

3.2.2 *Chemical durability*

Under acidic conditions, as found, e.g. inside macrophages, lanthanide oxides, Ln_2O_3, suffer from a poor chemical durability [53] resulting in their dissolution and formation of free lanthanide ions. The chemical durability of the obtained Gd_2O_3:Er^{3+},Yb^{3+} nanostructures was investigated by adjusting the pH of an aqueous nanostructure dispersion to 3.0 with HCl. The change in pH was recorded as a function of time. Generally, in the presence of HCl, metal oxides react to metal chloride and water (Eq. 1). $GdCl_3$ is soluble in water leading to the formation of Gd^{3+} and Cl^- ions. During this reaction H^+ ions are consumed and consequently the reaction is accompanied by an increase in pH of the reaction medium. Further, most lanthanide oxides react spontaneously with water to lanthanide hydroxides (Eq. 2) [54]. The partial dissociation of $Gd(OH)_3$ in aqueous media results in the formation of Gd^{3+} as well as OH^- ions leading to an increase in pH ($pK_a(Gd(OH)_3) = 9.4$, $pK_b(Gd(OH)_3) = 5.7$). Therefore, the chemical durability of the nanostructures can be evaluated based on the change in pH of the solution, whereas an increase in pH of the nanostructure suspension indicates the partial dissolution of Gd_2O_3.

$$Gd_2O_3 + 6H^+ + 6Cl^- \rightarrow 2Gd^{3+} + 6Cl^- + 3H_2O \quad (1)$$

$$Gd_2O_3 + 3H_2O \rightarrow 2Gd(OH)_3 \rightarrow 2Gd^{3+} + 6OH^- \quad (2)$$

As obvious from Fig. 6, the immediate increase of the pH from initial 3.0 to a saturation value of 6.4 confirms the poor chemical durability of bare Gd_2O_3 nanostructures. On the other hand, after modification with PEG-*b*-PAAc particles and rods show good chemical durability.

3.3 In vitro cytotoxicity

In our previous work, the in vitro cytotoxicity of Gd_2O_3:Er^{3+},Yb^{3+} nanostructures towards B-cell hybridomas and macrophages was investigated by a set of cytotoxicity assays [38, 55]. Briefly, we found no cytotoxic

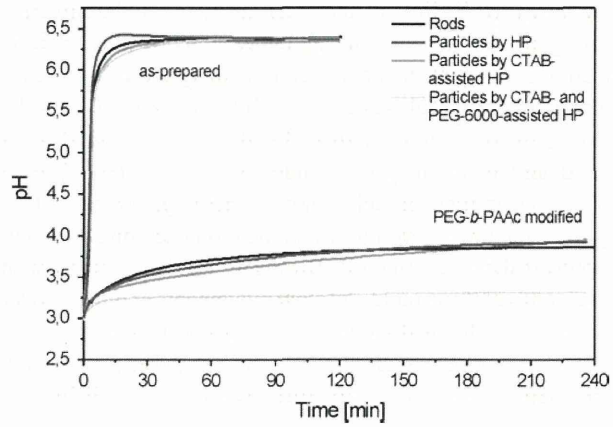

Fig. 6 Chemical durability of bare and PEG-*b*-PAAc modified Gd_2O_3:Er^{3+},Yb^{3+} nanostructures

effect after incubation of up to 500 μg/mL Gd_2O_3:Er^{3+},Yb^{3+} with B-cells hybridomas, but low viabilities have been observed in case of macrophages (Fig. 7a). The cytotoxic effect is deduced to the uptake of the nanostructures by macrophages, followed by a partial dissolution and release of toxic Gd^{3+} ions due to the poor chemical durability of gadolinium oxide under acidic conditions inside macrophages. Surface modification with PEG-*b*-PAAc improves the chemical durability of the nanostructures, resulting in viabilities of macrophages that are at least 20–40 % higher than the viabilities of cell cultures incubated with bare nanostructures (Fig. 7b, c).

Besides the improved chemical durability of modified Gd_2O_3:Er^{3+},Yb^{3+}, changes in the surface properties have been suggested as a potential reason for the observed biocompatibility after PEG-*b*-PAAc modification. It is known that the interaction between cells and nanostructured materials depends not only on size and morphology but also on surface charge [56]. Due to the generally negatively charged cell membrane, nanostructures with a positive surface charge should be uptaken more easily than those with a negative surface charge. Measurement of the ζ-potential of bare and PEG-*b*-PAAc modified nanostructures revealed a positive surface charge before, a negative surface charge after modification. Consequently, a higher incorporation rate, and therefore lower viability, is expected for bare nanostructures when compared to modified Gd_2O_3:Er^{3+},Yb^{3+}. For verification, bare and PEG-*b*-PAAc modified Gd_2O_3:Er^{3+},Yb^{3+} nanorods and nanoparticles (CTAB-assisted HP, d ~ 160 nm) have been incubated with macrophages, followed by investigation in CLSM.

3.4 In vitro cellular uptake (CLSM)

In order to monitor the in vitro cellular uptake of Gd_2O_3:Er^{3+},Yb^{3+} nanostructures by macrophages as a function of surface modification, we used CLSM. Bare and PEG-*b*-PAAc modified nanorods and particles (160 nm) were incubated with macrophages for 12 h, followed by fixation of the cells. Cytoplasm was stained with CellTracker Orange (CMRA), which emits in orange range (576 nm) under 543-nm excitation. Blue (461 nm, λ_{ex} = 760 nm) emitting DAPI was used to stain the nucleus. Under 980-nm excitation green (550 nm) and red (670 nm) upconversion emission from Gd_2O_3:Er^{3+},Yb^{3+} can be detected in CLSM allowing the localization of the nanostructures (Fig. 8).

In case of bare nanoparticles obtained by CTAB-assisted HP (Fig. 8a), red and green upconversion emission was detected in cytoplasm confirming the uptake of

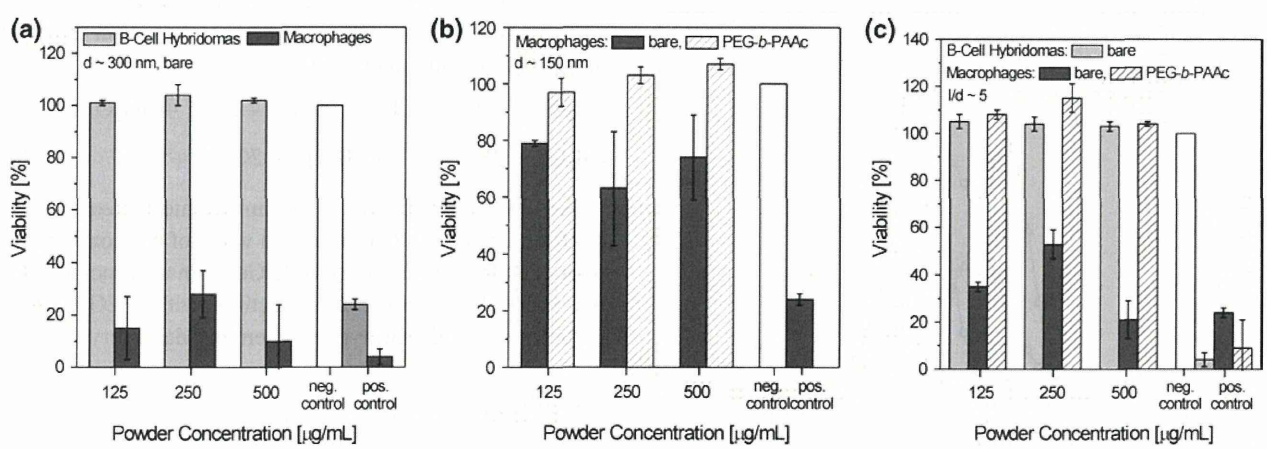

Fig. 7 In vitro cytotoxicity determined by trypan blue assay. **a** Viability of B-cell hybridomas (incubation time 48 h) and macrophages (incubation time 24 h) after incubation with bare particles obtained by homogeneous precipitation. **b** Viability of macrophages incubated with bare and PEG-*b*-PAAc modified particles obtained by surfactant assisted HP (incubation time 24 h). **c** Viability of bare and PEG-*b*-PAAc modified nanorods incubated with B-cell hybridomas and macrophages (incubation time 24 h). Negative control: medium alone. Positive control: carboplatin

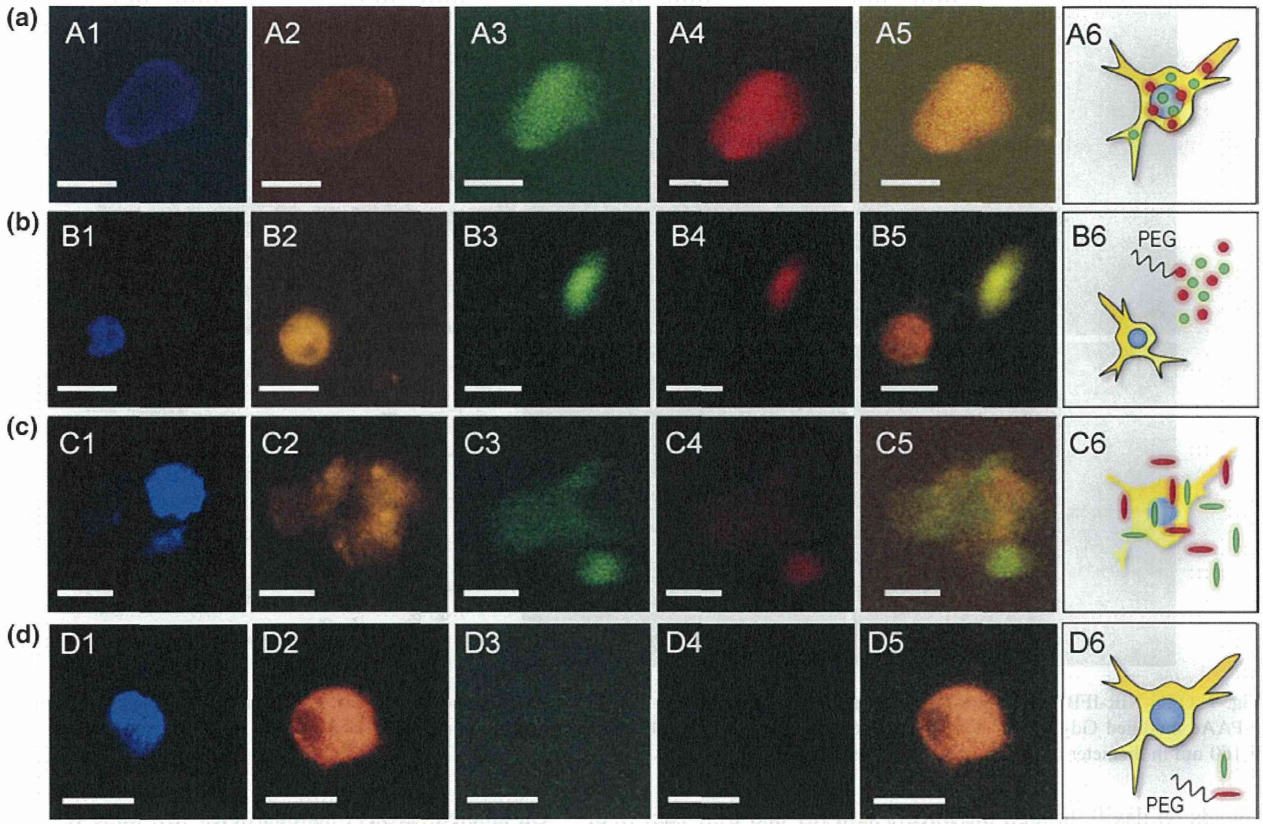

Fig. 8 CLSM images of macrophages incubated with **a** bare and **b** PEG-*b*-PAAc modified particles as well as **c** bare and **d** PEG-*b*-PAAc modified rods. *Scale bar* 10 μm. *1* DAPI stained nucleus ($\lambda_{ex} = 760$ nm, $\lambda_{em} = 461$ nm). *2* CMRA stained cytoplasm ($\lambda_{ex} = 543$ nm, $\lambda_{em} = 576$ nm). *3* Green (550 nm) and *4* red (670 nm) upconversion emission of Gd_2O_3:Er^{3+},Yb^{3+} under 980-nm excitation. *5* Overlay. *6* Schematic representation

Gd_2O_3:Er^{3+},Yb^{3+} by the macrophage. After modification with PEG-*b*-PAAc (Fig. 8b) no upconversion signal is detected in the cytoplasm but next to macrophage. This observation indicates that PEG-*b*-PAAc modified particles have not been taken up by the cell. Further, the observation of healthy macrophages is in agreement with the high viability of macrophages incubated with modified nanostructures determined by trypan blue assay (Fig. 7b). As obvious from Fig. 8c, green and red luminescence emitted from bare nanorods can be detected in and around cytoplasm of the presented dead macrophage revealing the cytotoxic effect (Fig. 7c) and cellular uptake of bare Gd_2O_3:Er^{3+},Yb^{3+} nanorods. Macrophages incubated with PEG-*b*-PAAc modified nanorods are in healthy configuration. Only week green upconversion emission could be detected outside cytoplasm (Fig. 8d). These results confirm the cellular uptake of bare Gd_2O_3:Er^{3+},Yb^{3+}. On the other hand, less nanostructures with PEG-*b*-PAAc modification have been uptaken by macrophages. This is in agreement with the reduction of non-specific uptake by macrophages reported for PEG-modified nanostructures, such as iron oxide or poly(lactic acid) (PLA) nanoparticles [57–59]. The results obtained from in vitro cytotoxicity assays and observations made in CLSM show that the introduction of a PEG-*b*-PAAc shell on the gadolinium oxide core structure provides good biocompatibility under studied conditions. This fact can be assigned first to an improved chemical durability under acid conditions and second to a PEG-*b*-PAAc-induced decrease in cellular uptake.

3.5 In vivo distribution of PEG-*b*-PAAc modified Gd_2O_3:Er^{3+},Yb^{3+}

The in vivo distribution of PEG-*b*-PAAc modified Gd_2O_3:Er^{3+},Yb^{3+} nanostructures was investigated by using C57BL/6 mice. Nanostructures were suspended in HEPES buffer at 500 μg/mL concentration and were injected through tail vein (2.5 mg Gd_2O_3:Er^{3+},Yb^{3+} per mouse). After a few hours (day-0-mice), respectively 24 h (day-1-mice) mice have been killed and nanostructure distribution was observed in the OTN-NIR-FIB system NIS-Opt. Figure 9 shows the NIR emission intensity under 980-nm excitation on day 0 and day 1. Mice treated with particles of 210 and 160 nm diameter show intensive

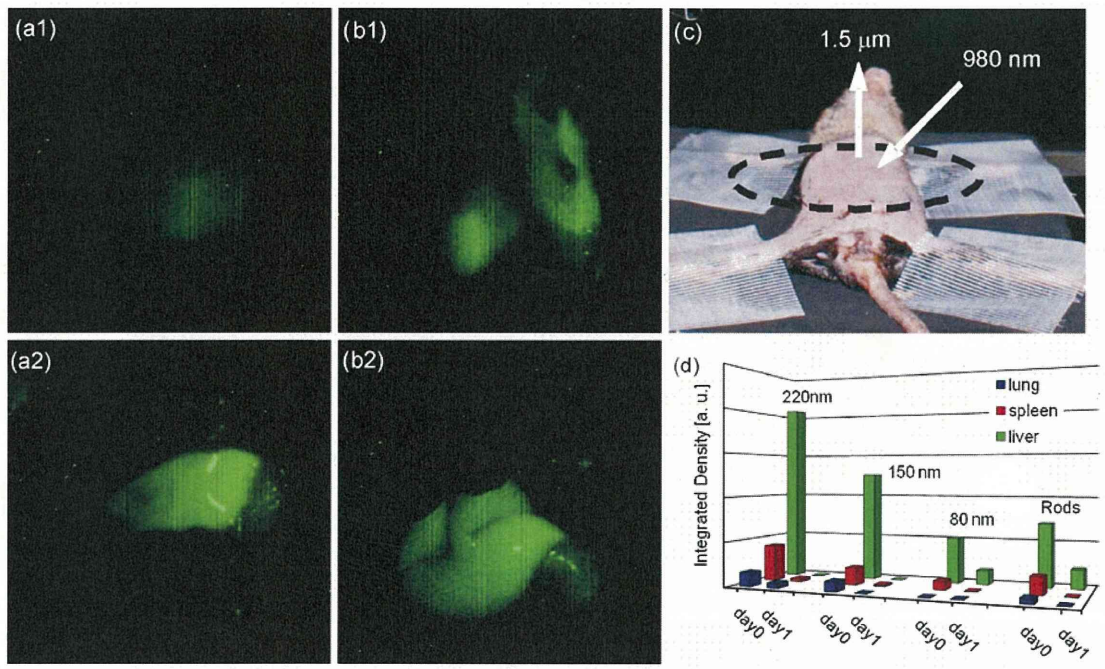

Fig. 9 OTN-NIR-IFBI false-color images of mice treated with PEG-*b*-PAAc modified Gd_2O_3:Er^{3+},Yb^{3+} nanoparticles of **a** 210 nm and **b** 160 nm in diameter (*1* whole body, *2* opened body, day-0-mouse). **c** Investigated body part. **d** NIR emission intensity (integrated density) from lung, liver and spleen of day-0- and day-1-mice. $P_{Laser} = 4.5$ W, $\lambda_{ex} = 980$ nm, $\lambda_{em} = 1.5$ μm

signals on day 0 through the mice's skin (a1 and b1). The signal is originating from Gd_2O_3:Er^{3+},Yb^{3+} particles accumulated in the liver as confirmed by observation of the dissected mice (a2 and b2). In case of smaller particles and nanorods, no signal was detected from the whole body, but the accumulation of nanostructures was confirmed by investigating single organs (Fig. 9d) as well as histological sections of liver, lung, spleen and kidneys (Fig. 10).

The organ biodistribution study on day 0 reveals that the nanostructures were mainly distributed in liver, spleen and lung. Herein, signal intensity decreased with decreasing particle diameter from 210 to 85 nm. The emission intensity in case of nanorods is in between those intensities measured for 85 and 160 nm particles (Fig. 9d). NIR–NIR upconversion emission signals from organs of day-1-mice reveal a strong decrease in signal intensity suggesting the clearance of the nanostructures throughout the time course of this study. Fluorescence microscopic analysis of histological sections taken from liver, spleen, lung and kidney reveals a similar trend (Fig. 10e). Strongest NIR emission is detected from spleen and liver, whereas the signal intensity decreases from largest particles (210 nm, surfactant-free HP) to nanorods and smallest particles (85 nm, CTAB- and PEG-6.000-assisted HP).

The uptake of nanostructures by clearance organs (liver and spleen) and lung has been reported for various nanoprobes for biomedical applications [60–62]. Gratton et al. [63] investigated the uptake and elimination of ^{64}Cu-labeled DOTA-nanoparticles by time-resolved MicroPET imaging. According to the authors, the accumulation in clearance organs and the short elimination time after injection indicates the quick recognition of nanostructures as foreign followed by the removal from systemic circulation by the reticuloendothelial system (RES). Herein, Kupffer cells play a central role as shown by Danscher et al. [64]. The authors reported the uptake of 2 and 40 nm gold nanoparticles primarily by Kupffer cells in the liver and secondarily by macrophages in the spleen. Kryza et al. [65] reported the free circulation of less than 5 nm in diameter Gd_2O_3 nanoparticles with a polysiloxane shell in the blood without RES uptake, and observed renal elimination of the nanostructures by SPECT, MR and optical imaging. Silicon quantum dots are reported to accumulate in the urinary bladder as well as the liver and are excreted via renal filtration shortly after injection, whereas the main site for accumulation of remaining quantum dots 48 h after injection is the liver [66]. In our study, fluorescence microscopic analysis of urine samples taken from day-0- and day-1-mice injected with 85 and 160 nm particles showed a low content of green and NIR upconverting Gd_2O_3:Er^{3+},Yb^{3+} particles of 160 nm in diameter. Further NIR emission was detected from histological sections of the kidneys (Fig. 10e). This observation suggests minor renal elimination of the nanostructures from the body. However, based on obtained OTN-NIR-FIB images and due to nanostructures size [67] from 85 to

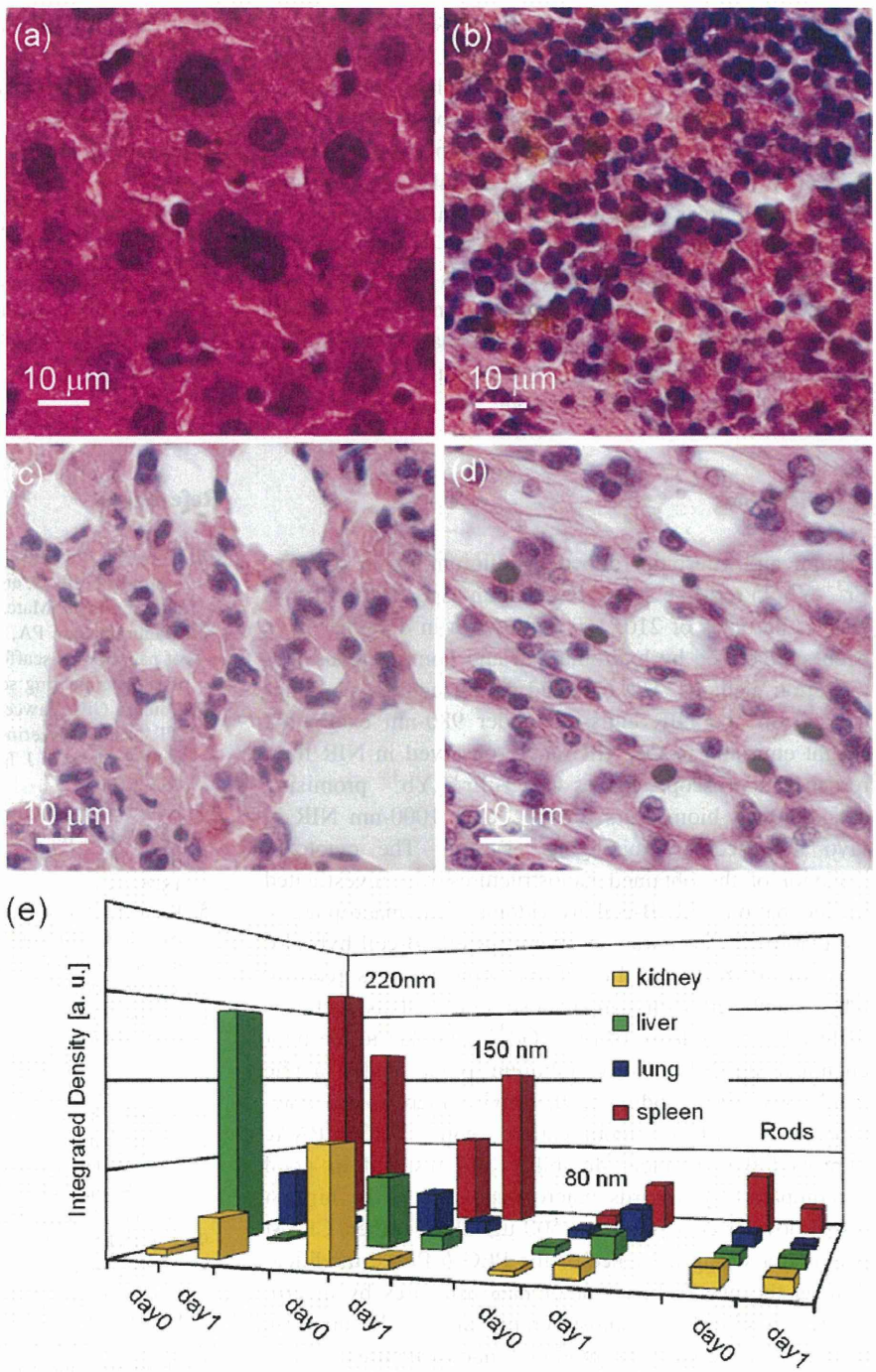

Fig. 10 Histological sections (*violet*: haematoxylin staining of the nuclei, *red*: eosin staining of eosinophilic structures such as intracellular or extracellular proteins including cytoplasm and red blood cells) of **a** liver, **b** spleen, **c** lung and **d** kidney of day-0-mice treated with 210 nm particles as well as **e** NIR emission intensity (integrated density) from histological sections of day-0- and day-1-mice's organs (P_{Laser} = 650 mW, λ_{ex} = 980 nm, λ_{em} = 1.5 µm)

210 nm, uptake by Kupffer cells in the liver and macrophages in the spleen is proposed to be the main clearance mechanism. Hereby it must be taken into account that those results clearly show the existence of Gd_2O_3:Er^{3+},Yb^{3+} nanostructures in lung, liver, spleen and kidney. However, a potential biodistribution in other organs cannot be completely ruled out as the lower detection limit of this newly developed in vivo NIR-based imaging system is still unclear. The lower limit is still remained to be researched and further investigations including the confirmation of the biodistribution by methods such as ICP-MS are recently underway.

The influence of geometry and surface charge on biodistribution was studied by Arnida et al. [68]. A reduced uptake of PEGylated gold nanorods by macrophages was compared to PEGylated nanoparticles. Nanoparticles of

negative surface charge accumulated in the liver at notably higher extent than nanorods of almost neutral charge, which was deduced to different morphology and surface charge. We observed reduced NIR emission from organs of mice treated with nanorods, which may be, in accordance to Armida et al., due to a reduced accumulation of rod-like structures in liver, spleen and lung when compared to nanoparticles. As both of our PEG-*b*-PAAc modified Gd_2O_3:Er^{3+},Yb^{3+} nanostructures, rods and particles, exhibit a negative surface charge, the influence of morphology may be more important than that of the surface charge and a morphology driven accumulation and blood circulation time cannot be ruled out.

4 Conclusions

Erbium and ytterbium doped gadolinium oxide (Gd_2O_3:Er^{3+},Yb^{3+}) rod-like structures with an aspect ratio of 5 as well as particles of 210, 160 and 85 nm in diameter have been synthesized by hydrothermal and homogeneous precipitation methods. The obtained nanostructures show upconversion and NIR emission under 980-nm excitation. Bright emission in the NIR range, observed in NIR fluorescence microscope, makes Gd_2O_3:Er^{3+},Yb^{3+} promising candidates as biomarkers for the "over 1000-nm NIR in vivo fluorescence bioimaging" system. The cytotoxic behavior of the obtained nanostructures was investigated by incubation with B-cell hybridomas and macrophages. No cytotoxic effect was observed towards B-cell hybridomas. In contrast, viability of macrophages was reduced when incubated with bare nanostructures. This fact was deduced to the release of toxic Gd^{3+} ions due to the poor chemical durability of gadolinium oxide under acidic conditions corresponding to the environment inside macrophages. Surface modification with PEG-*b*-PAAc improved the chemical durability and resulted in good biocompatibility towards macrophages up to the highest tested powder concentration (500 μg/mL). Further, CLSM revealed a strong influence of the PEG-*b*-PAAc modification on the uptake behavior of nanostructures by macrophages. While bare nanostructures are easily uptaken, tendency for uptake of modified nanostructures is less pronounced. This observation is assigned to the change in surface charge from positive to negative range by introduction of PEG-*b*-PAAc chains on the nanostructure surface. The in vivo distribution of PEG-*b*-PAAc modified nanostructures in mouse organs was investigated in the OTN-NIR-IFBI system, revealing nanostructures in clearance organs (liver, kidneys and spleen) and lung. Most intensive emission was detected from particles larger than 100 nm. Histological sections of the organs confirmed those results. Further, elimination studies in fluorescence microscope suggest the clearance of the nanostructures via liver and kidneys. The observed biocompatibility and strong UPC as well as NIR emission under 980-nm excitation make those PEG-*b*-PAAc modified Gd_2O_3:Er^{3+},Yb^{3+} nanoparticles and rods promising candidates for NIR bioimaging.

Acknowledgment This work was partly supported by Matching Fund Subsidy from MEXT (Ministry of Education, Culture, Sports, Science and Technology), 2006–2010 and 2009–2013. The authors thank Dr. Lionel Vayssieres (WPI Center for Materials NanoArchitectonics (MANA), National Institute for Materials Science (NIMS), Tsukuba, Japan) for scientific discussion and provision of the zeta-potential equipment.

References

1. Hong YL, Fan HS, Li B, Guo B, Liu M, Zhang XD. Fabrication, biological effects, and medical applications of calcium phosphate nanoceramics. Mater Sci Eng R. 2010;70:225–42.
2. Madurantakam PA, Cost CP, Simpson DG, Bowlin GL. Science of nanofibrous scaffold fabrication: strategies for next generation tissue-engineering scaffolds. Nanomedicine. 2009;4:193–206.
3. Poinern GEJ, Fawcett D, Ng YJ, Ali N, Brundavanam RK, Jiang ZT. Nanoengineering a biocompatible inorganic scaffold for skin wound healing. J Biomed Nanotechnol. 2010;6(Special issue): 497–510.
4. Kallinteri P, Higgins S, Hutcheon GA, St Pourcain CB, Garnett MC. Novel functionalized biodegradable polymers for nanoparticle drug delivery systems. Biomacromolecules. 2005;6: 1885–94.
5. Kreuter J, Shamenkov D, Petrov V, Ramge P, Cychutek K, Koch-Brandt C, Alyautdin R. Apolipoprotein-mediated transport of nanoparticle-bound drugs across the blood-brain barrier. J Drug Target. 2002;10:317–25.
6. Hughes GA. Nanostructure-mediated drug delivery. Nanomedicine. 2005;1:22–30.
7. Tosi G, Costantino L, Rivasi F, Ruozi B, Leo E, Vergoni AV, Tacchi R, Bertolini A, Vandelli MA, Forni F. Targeting the central nervous system: in vivo experiments with peptide-derivatized nanoparticles loaded with Loperamide and Rhodamine-123. J Control Release. 2007;122:1–9.
8. Ravi Kumar MNV. Nano and microparticles as controlled drug delivery devices. J Pharm Pharm Sci. 2000;3:234–58.
9. Yan E, Fu Y, Wang X, Ding Y, Qian H, Wang CH, Hu Y, Jiang X. Hollow chitosan-silica nanospheres for doxorubicin delivery to cancer cells with enhanced antitumor effect in vivo. J Mater Chem. 2011;21:3147–55.
10. Rosenblum LT, Kosaka N, Mitsunaga M, Choyke PL, Kobayashi H. In vivo molecular imaging using nanomaterials: general in vivo characteristics of nano-sized reagents and applications for cancer diagnosis (review). Mol Membr Biol. 2010;27:274–85.
11. Corr SA, Rakovich YP, Gun'ko YK. Multifunctional magnetic-fluorescent nanocomposites for biomedical applications. Nanoscale Res Lett. 2008;3:87–104.
12. Pautler M, Brenner S. Nanomedicine: promises and challenges for the future of public health. Int J Nanomed. 2010;5:803–9.
13. Portney NG, Ozkan M. Nano-oncology: drug delivery, imaging, and sensing. Anal Bioanal Chem. 2006;384:620–30.
14. Kotov NA, Winter JO, Clements IP, Jan E, Timko BP, Campidelli S, Pathak S, Mazzatenta A, Lieber CM, Prato M, Bellamkonda RV, Silva GA, Wong Shi Kam N, Patolsky F, Ballerini

L. Nanomaterials for neural interfaces. Adv Mater. 2009;21: 3970–4004.
15. Shaner NC, Lin MZ, McKeown MR, Steinbach PA, Hazelwood KL, Davidson MW, Tsien RY. Improving the photostability of bright monomeric orange and red fluorescent proteins. Nat Methods. 2008;5:545–51.
16. Chudakov DM, Matz MV, Lukyanov S, Lukyanov KA. Fluorescent proteins and their applications in imaging living cells and tissues. Physiol Rev. 2010;90:1103–63.
17. Michalet X, Pinaud FF, Bentolila LA, Tsay JM, Doose S, Li JJ, Sundaresan G, Wu AM, Gambhir SS, Weiss S. Science. 2005; 307:538–44.
18. Sharma P, Brown S, Walter G, Santra S, Moudgil B. Nanoparticles for bioimaging. Adv Colloid Interface Sci. 2006;123–126:471–85.
19. Lu Z, Zhu Z, Zheng X, Qiao Y, Guo J, Li CM. Biocompatible fluorescence-enhanced ZrO_2-CdTe quantum dot nanocomposite for in vitro cell imaging. Nanotechnology. 2011;22:155604.
20. Vela J, Htoon H, Chen Y, Park YS, Ghosh Y, Goodwin PM, Werner JH, Wells NP, Casson JL, Hollingsworth JA. Effect of shell thickness and composition on blinking suppression and the blinking mechanism in 'giant' CdSe/CdS nanocrystal quantum dots. Biophotonics. 2010;3:706–17.
21. Frantsuzov PA, Marcus RA. Explanation of quantum dot blinking without the long-lived trap hypothesis. Phys Rev B. 2005;72:155321.
22. Cotton S. Lanthanide and actinide chemistry. Chichester: Wiley; 2006.
23. Hanaoka K. Development of responsive lanthanide-based magnetic resonance imaging and luminescent probes for biological applications. Chem Pharm Bull. 2010;58:1283–94.
24. Andraud C, Maury O. Lanthanide complexes for nonlinear optics: from fundamental aspects to applications. Eur J Inorg Chem. 2009;29–30:4357–71.
25. Das GK, Heng BC, Ng SC, White T, Loo JSC, D'Silva L, Padmanabhan P, Bhakoo KK, Selvan ST, Tan TTY. Gadolinium oxide ultranarrow nanorods as multimodal contrast agents for optical and magnetic resonance imaging. Langmuir. 2010;26: 8959–65.
26. Pang M, Liu D, Lei Y, Song S, Feng J, Fan W, Zhang H. Rare-earth-doped bifunctional alkaline-earth metal fluoride nanocrystals via a facile microwave-assisted process. Inorg Chem. 2011; 50:5327–9.
27. Kamimura M, Miyamoto D, Saito Y, Soga K, Nagasaki Y. Design of poly(ethylene glycol)/streptavidin coimmobilized upconversion nanophosphors and their application to fluorescence biolabeling. Langmuir. 2008;24:8864–70.
28. Xiong L, Chen Z, Tian Q, Cao T, Xu C, Li F. High contrast upconversion luminescence targeted imaging in vivo using peptide-labeled nanophosphors. Anal Chem. 2009;81:8687–94.
29. Anderson RR, Parrish JA. The optics of human skin. J Invest Dermatol. 1981;77:13–9.
30. Hilderbrand SA, Shao F, Salthouse C, Mahmood U, Weissleder R. Upconverting luminescent nanomaterials: application to in vivo bioimaging. Chem Commun. 2009;28:4188–90.
31. Nyk M, Kumar R, Ohulchanskyy TY, Bergey EJ, Prasad PN. High contrast in vitro and in vivo photoluminescence bioimaging using near infrared to near infrared up-conversion in Tm3+ and Yb3+ doped fluoride nanophosphors. Nano Lett. 2008;8:3834–8.
32. Kumar R, Nyk M, Ohulchanskyy TY, Flask CA, Prasad PN. Combined optical and MR bioimaging using rare earth ion doped NaYF4 nanocrystals. Adv Funct Mater. 2009;19:853–9.
33. Chen G, Ohulchanskyy TY, Law WC, Agren H, Prasad PN. Monodisperse $NaYbF_4$: Tm^{3+}/$NaGdF_4$ core/shell nanocrystals with near-infrared to near-infrared upconversion photoluminescence and magnetic resonance properties. Nanoscale. 2011;3:2003–8.
34. Zhou J, Sun Y, Du X, Xiong L, Hu H, Li F. Dual-modality in vivo imaging using rare-earth nanocrystals with near-infrared to near-infrared (NIR-to-NIR) upconversion luminescence and magnetic resonance properties. Biomaterials. 2010;31:3287–95.
35. Troyan SL, Kianzad V, Gibbs-Strauss SL, Gioux S, Matsui A, Oketokoun R, Ngo L, Khamene A, Azar F, Frangioni JV. The FLARE intraoperative near-infrared fluorescence imaging system: a first-in-human clinical trial in breast cancer sentinel lymph node mapping. Ann Surg Oncol. 2009;16:2943–52.
36. Vahrmeijer AL, Frangioni JV. Seeing the invisible during surgery. Br J Surg. 2011;98:749–50.
37. Soga K, Tokuzen K, Tsuji K, Yamano T, Hyodo H, Kishimoto H. NIR bioimaging: development of liposome-encapsulated, rare-earth-doped Y2O3 nanoparticles as fluorescent probes. Eur J Inorg Chem. 2010;18:2673–7.
38. Hemmer E, Yamanao T, Kishimoto H, Soga K. Gadolinium-containing inorganic nanostructures for biomedical applications: cytotoxic aspects. In: IEEE Explore, proceedings of the international conference on nanoscience and nanotechnology (ICONN), Sydney, Australia; 2010. p. 225–9.
39. Singh S, Bhat MK. Carboplatin induces apoptotic cell death through downregulation of constitutively active nuclear factor-jB in human HPV-18 E6-positive HEp-2 cells. Biochem Biophys Res Commun. 2004;318:346–53.
40. Farrer RA, Butterfield FL, Chen VW, Fourkas JT. Highly efficient multiphoton-absorption-induced luminescence from gold nanoparticles. Nano Lett. 2005;5:1139–42.
41. Matijevic E, Hsu WP. Preparation and properties of monodispersed colloidal particles of lanthanide compounds. J Colloid Interface Sci. 1987;118:506–23.
42. Park IY, Kim D, Lee J, Lee SH, Kim KJ. Effects of urea concentration and reaction temperature on morphology of gadolinium compounds prepared by homogeneous precipitation. Mater Chem Phys. 2007;106:149–57.
43. Wang Y, Bai X, Liu T, Dong B, Xu L, Liu Q, Song H. Solvothermal synthesis and luminescence properties of monodisperse Gd_2O_3:Eu^{3+} and Gd_2O_3:Eu^{3+}@SiO_2 nanospheres. J Solid State Chem. 2010;183:2779–85.
44. Mu Q, Chen T, Wang Y. Synthesis, characterization and photoluminescence of lanthanum hydroxide nanorods by a simple route at room temperature. Nanotechnology. 2009;20:345602.
45. Lin S, Dong X, Jia R, Yuan Y. Controllable synthesis and luminescence property of $LnPO_4$ (Ln = La, Gd, Y) nanocrystals. J Mater Sci Mater Electron. 2010;21:38–44.
46. Du G, Van Tendeloo G. Preparation and structure analysis of $Gd(OH)_3$ nanorods. Nanotechnology. 2005;16:595–7.
47. Wang X, Li Y. Synthesis and characterization of lanthanide hydroxide single-crystal nanowires. Angew Chem Int Ed. 2002;41:4790–3.
48. Wang X, Li Y. Solution-based routes to transition-metal oxide one-dimensional nanostructures. Pure Appl Chem. 2006;78: 45–64.
49. Ma L, Chen WX, Zhao J, Zheng YF. Synthesis of $Pr(OH)_3$ and Pr_6O_{11} nanorods by microwave-assisted method: effects of concentration of alkali and microwave heating time. J Cryst Growth. 2007;303:590–6.
50. Venkatachalam N, Saito Y, Soga K. Synthesis of Er^{3+} doped Y_2O_3 nanophosphors. J Am Ceram Soc. 2009;92:1006–10.
51. Günther A, Bender P, Birringer R. Rotational diffusion of magnetic nickel nanorods in colloidal dispersions. J Phys Condens Matter. 2011;23:325103.
52. Mahler H-C, Jiskoot W. Analysis of aggregates and particles in protein pharmaceuticals. Hoboken: Wiley; 2012. p. 44.
53. Soga K, Okumura Y, Tsuji K, Venkatachalam N. Effect of K_3PO_4 addition as sintering inhibitor during calcination of Y_2O_3 nanoparticles. J Phys Conf Ser. 2009;191:012003.
54. Wang X, Li Y. Rare-earth-compound nanowires, nanotubes, and fullerene-like nanoparticles: synthesis, characterization, and properties. Chem Eur J. 2003;9:5627–35.

55. Hemmer E, Yamano T, Kishimoto H, Soga K. Cytotoxicity of Gd_2O_3:Ln^{3+} nanostructures and their potential as biomarkers. In: Meyer G, editor. Proceedings of the 7th international conference on f elements, ICfE-7, Terrae Rarae; 2009. p. 1–10.
56. Dong Y, Feng SS. Methoxy poly(ethylene glycol)-poly(lactide) (MPEG-PLA) nanoparticles for controlled delivery of anticancer drugs. Biomaterials. 2004;25:2843–9.
57. Xie J, Xu C, Kohler N, Hou Y, Sun S. Controlled PEGylation of monodisperse Fe_3O_4 nanoparticles for reduced non-specific uptake by macrophage cells. Adv Mater. 2007;19:3163–6.
58. Sheng Y, Yuan Y, Liu C, Tao X, Shan X, Xu F. In vitro macrophage uptake and in vivo biodistribution of PLA-PEG nanoparticles loaded with hemoglobin as blood substitutes: effect of PEG content. J Mater Sci Mater Med. 2009;20:188–891.
59. Bazile D, Prud'Homme C, Bassoullet MT, Marlard M, Spenlehauer G, Veillard M. Stealth Me.PEG-PLA nanoparticles avoid uptake by the mononuclear phagocytes system. J Pharm Sci. 1995;84:493–8.
60. Wu H, Liu G, Zhuang Y, Wu D, Zhang H, Yang H, Hu H, Yang S. The behavior after intravenous injection in mice of multiwalled carbon nanotube/Fe_3O_4 hybrid MRI contrast agents. Biomaterials. 2011;32:4867–76.
61. Al Faraj A, Fauvelle F, Luciani N, Lacroix G, Levy M, Crémillieux Y, Canet-Soulas E. In vivo biodistribution and biological impact of injected carbon nanotubes using magnetic resonance techniques. Int J Nanomed. 2011;6:351–61.
62. Tasciotti E, Godin B, Martinez JO, Chiappini C, Bhavane R, Liu X, Ferrari M. Near-infrared imaging method for the in vivo assessment of the biodistribution of nanoporous silicon particles. Mol Imaging. 2011;10:56–68.
63. Gratton SEA, Williams S, Napier ME, Pohlhaus PD, Zhou Z, Wiles KB, Maynor BW, Shen C, Olafsen T, Samulski ET, DeSimone JM. The pursuit of a scalable nanofabrication platform for the use in material and life science applications. Acc Chem Res. 2008;41:1685–95.
64. Sadauskas E, Wallin H, Stoltenberg M, Vogel U, Doering P, Larsen A, Danscher G. Kupffer cells are central in the removal of nanoparticles from the organism. Particle Fibre Toxicol. 2007;4:10.
65. Kryza D, Taleb J, Janier M, Marmuse L, Miladi I, Bonazza P, Louis C, Perriat P, Roux S, Tillement O, Billotey C. Biodistribution study of nanometric hybrid gadolinium oxide particles as a multimodal SPECT/MR/optical imaging and theragnostic agent. Bioconjug Chem. 2011;22:1145–52.
66. Tu C, Ma X, House A, Kauzlarich SM, Louie AY. PET imaging and biodistribution of silicon quantum dots in mice. ACS Med Chem Lett. 2011;2:285–8.
67. Nagayama S, Ogawara K, Fukuoka Y, Higaki K, Kimura T. Time-dependent changes in opsonin amount associated on nanoparticles alter their hepatic uptake characteristics. Int J Pharm. 2007;342:215–21.
68. Arnida, Janát-Amsbury MM, Ray A, Peterson CM, Ghandehari H. Geometry and surface characteristics of gold nanoparticles influence their biodistribution and uptake by macrophages. Eur J Pharm Biopharm. 2011;77:417–23.